Special Issue: Continuous-Discontinuous Long Fiber-Reinforced Polymer Composite Structures

JOURNAL OF THERMOPLASTIC COMPOSITE MATERIALS

Journal of Thermoplastic Composite Materials
2024, Vol. 0(0) 1–31

DOI: 10.1177/08927057241296472
journals.sagepub.com/home/jtc
Sage

Crystallization and crystal morphology of polymers: A multiphase-field study

Navid Afrasiabian[1], Ahmed Elmoghazy[2], Juliane Blarr[3], Benedikt Scheuring[3], Andreas Prahs[2], Daniel Schneider[4,5], Wilfried V Liebig[3], Kay A Weidenmann[6], Colin Denniston[1] and Britta Nestler[2,4,5]

Abstract

In this paper, we introduce a coarse-grained model of polymer crystallization using a multiphase-field approach. The model combines a multiphase-field method, Nakamura's kinetic equation, and the equation of heat conduction for studying microstructural evolution of crystallization under isothermal and non-isothermal conditions. The multiphase-field method provides flexibility in adding any number of phases with different properties making the model effective in studying blends or composite materials. We apply our model to systems of neat PA6 and study the impact of initial distribution of crystalline grains and cooling rate on the morphology of the system. The relative crystallinity (conversion) curves show qualitative agreement with experimental data. We also investigate the impact of including carbon fibers on the crystallization and grain morphology. We observe a more homogeneous crystal morphology around fibers. This is associated with the higher initial volume fraction of crystal grains and higher heat

[1]Department of Physics and Astronomy, Univeristy of Western Ontario, London, ON, Canada
[2]Institute for Applied Materials - Microstructure Modeling and Simulation, Karlsruhe Institute of Technology (KIT), Karlsruhe, Germany
[3]Institute for Applied Materials - Materials Science and Engineering, Karlsruhe Institute of Technology (KIT), Karlsruhe, Germany
[4]Institute of Digital Materials Science (IDM), Karlsruhe University of Applied Sciences, Karlsruhe, Germany
[5]Institute of Nanotechnology (INT), Karlsruhe Institute of Technology (KIT), Karlsruhe, Germany
[6]Institute for Materials Resource Management, Hybrid Composite Materials, Augsburg University, Augsburg, Germany

Corresponding author:
Navid Afrasiabian, Department of Physics and Astronomy, Univeristy of Western Ontario, 1151 Richmond Street, London, ON N6A 3K7, Canada.
Email: nafrasia@uwo.ca

conductivity of the fiber (compared to the polymer matrix). Additionally, we observe that the crystalline grains at the fiber surface grow perpendicular to the surface. This indicates that the vertical growth observed in experiments is merely due to geometrical constraints imposed by the fiber surface and neighbouring crystalline regions.

Keywords
Multiphase-field, crystallization kinetics, fiber-reinforced polymer

Introduction

Polymer composites are widely used across various industries due to their enhanced mechanical properties, including high specific strength and durability, which often surpass those of bulk materials.[1–4] Their lightweight nature makes them particularly desirable in aerospace and automotive applications, enhancing fuel efficiency and overall performance. These composites typically consist of a polymer-based matrix and reinforcing materials such as fibers, particles, or nanofibers. Recently, semi-crystalline thermoplastics have become more common as the matrix material due to their ease of manufacture and recyclability. The properties of these products heavily depend on the formed morphology and degree of crystallization during manufacturing, making the study of crystallization kinetics and crystal morphology crucial.[4–8]

Recent modeling and applications

In recent years, there has been a considerable amount of numerical and computational attempts to model polymer crystallization at different scales, from single molecule to single crystal and beyond.[9] Monte Carlo simulations have been used to shed light on nucleation and growth of polymer single crystals as well as their morphology.[10,11] Kundagrami et al. presented a continuum kinetic model for crystal growth in polymers accounting for two crystallization regimes: nucleation controlled and diffusion controlled.[12]

Huang and Kamal presented a model for the morphological solidification of polymers.[13] Addressing the challenging multi-scale nature of polymer crystals and their complexities, they incorporated insights from phase-field and nucleation theories to set up their model. The model involved coupled equations of an envelope growth equation tracking spherulite boundaries and impingement, and a lamellar orientation equation replicating the Maltese cross morphology of the spherulites. The growth velocity of the envelope was determined by the Hoffman-Lauritzen (HL) equation and lamellar orientation was reproduced using the Frank equation.[14] To address nucleation, they embedded nucleation seeds and defined a critical nucleus radius larger than which nuclei would be stable and grow. The chain conformation effects in the initial crystallization stages were ignored in this model.

Molnar and coworkers introduced a probabilistic method of polymer crystal nucleation and growth.[15] The model, in conjunction with experimental data, was used to estimate spherulite size, distribution, and nucleus density in the absence and presence of nucleating agents. In their model, the growth front of the spherulites were not tracked and the conversion degree and spherulite size distribution was estimated based on the phase transition time. The conversion curves generated by their model under isothermal conditions showed good agreement with experimental results.

Phase-field models are a powerful tool to study free boundary problems and systems with different phases.[16–18] Xu et al. studied spatio-temporal growth of isotactic polystyrene single crystals during isothermal crystallization using a phase-field model.[19] Wang et al. introduced a phase-field model to study isothermal crystallization of polymer melts.[20] Their model was able to reproduce various single crystal morphologies such as dendritic, lamellar branching, faceted hexagonal, and spherulitic structures.

Bahloul et al. modified the phase-field model of Kobayashi[21] to account for crystallization characteristics of polymeric material and reproduce quantitatively accurate results.[7] The improvement to the Kobayashi model was made by modifying the mobility of the phase field model and the source term coefficient in the heat equation which were computed using Hoffman-Lauritzen (HL) theory. In their model, the phase-field equation was coupled to the heat equation through the bulk contribution of the free energy and the heat equation was coupled to the phase-field parameter through a source term. Anisotropy and noise were added to the interface to reproduce dendritic patterns of spherulites. The results for isothermal crystallization of isotactic polystyrene were compared to experiments[22,23] and quantitative agreement was found in a specific range of temperatures.

Polymers often show up in the industry in the form of composite materials due to improved functionality and performance. However, the addition of reinforcing components such as fibers affects the crystallization process. Therefore, new assumptions and methods are required in their modelling. Krause et al. studied the spherulitic growth of a fiber-reinforced polymer using computer simulations.[24] Mehl and Rebenfeld generalized the Avrami model to account for the influence of fibers in the presence of both thermal and athermal nucleation.[25,26] Benard et al. took on an analytical approach based on the geometric method of Avrami to study the impact of fiber inclusion on isothermal crystallization polymers.[27] Haudin and Chenot developed a set of differential equations based on the Avrami model.[28] This allowed them to numerically solve spherulite evolution in polymer injection molding without oversimplifying assumptions. They also studied the size distribution of the spherulites using their model. Later, they extended their model to long-fiber thermoplastic composites including the impact of fiber surface transcrystallinity.[29] Galeski et al. proposed an analytical model of crystallization kinetics for polymer composites with fibers and nanofibers.[30] Ruan and co-workers investigated the crystallization of short fiber-reinforced composites during the cooling phase by means of a multi-scale model that coupled the macroscopic heat equation to the mesoscopic crystal morphology.[6,31]

Motivation and originality

As mentioned above, microstructure and morphology have a direct impact on the physical and mechanical properties of the material. Therefore, understanding the evolution and distribution of these microstructures is imperative.

The previous attempts to reproduce crystallization at microstructure level are mostly based on Kobayashi based phase-field models or probabilistic Avrami-based models. In Kobayashi-based models, the order parameter describes the crystallinity. This allows for the development of models for spherulitic and dendritic growth but limits the application of such models to larger scales. Particularly, simulating systems with fibers becomes extremely costly as the fibers are several orders of magnitude larger than the dendritic branches. The probabilistic Avrami-based models generate randomly dispersed nuclei and model their evolution based on the Avrami equation. The main challenge for such models is tracking of the boundaries and their interaction, especially for multi-component systems.

In this work, the multiphase-field method (MPF) is coupled with the Nakamura model and the heat equation to model the crystallization of polymeric materials on a micro-structural length scale. The MPF is a generalization of the classical phase-field method to numerous locally present phases.[32] This readily allows for the inclusion of extra phases such as fibers and the study of their impact on the crystallization of the polymeric material. MPF has successfully been used to study mircostructral behaviour of materials.[33–36]

In our model, the phase-field order parameter defines the crystalline areas, whereas the crystallization kinetic, within a crystallizing phase, is governed by the Nakamura model. This allows for a more coarse-grained description of the system compared to models at spherulitic level but still accounts for the inhomogeneities at the meso-scale. Therefore, the crystal grains in our model are not single crystal spherulites but regions where crystallization occurs containing several spherulites. The dependency of crystallization on temperature is also accounted for through the Nakamura model and the crystallization rate constant (defined later).

Outline

In the Modeling and theory section, we describe our model and the equations involved. In the Experimental data and results section, we share the experimental findings of our Differential Scanning Calorimetry (DSC) and Polarized Light Microscopy (PLM). In the Numerical studies and results section, we discuss the numerical implementation of the model and details regarding numerical constants and parameters. This is followed by the results of our simulations and the comparisons to experimental data. We finally conclude the article with a summary of the model and the results.

Modeling and theory

The main objective of the present work is to address the non-locality of crystalline structure in semi-crystalline polymeric materials and composites. To achieve this, we use

a multiphase-field (MPF) method to follow the evolution of crystalline grains while the crystallinity of each grain evolves according to an Avrami-type model. In this section, we explain each theory and how they have been utilized to successfully reproduce the crystallization of polymeric materials.

Multiphase-field method

Free energy functional. In this work, we employ a multiphase-field method to track the evolution of the crystalline phase. The starting point of the modeling is given by the free energy functional

$$\mathcal{F}(\boldsymbol{\phi}, \nabla\boldsymbol{\phi}, \chi) = \int_V f(\boldsymbol{\phi}, \nabla\boldsymbol{\phi}, \chi)\, \mathrm{d}V. \tag{1}$$

here, f denotes the free energy density and ϕ is the tuple of order parameters, i.e., $\phi = \{\phi_1, \ldots, \phi_N\}$, where N is the number of phases. The tuple of the gradients of the order parameters is abbreviated by $\nabla\phi = \{\nabla\phi_1, \ldots, \nabla\phi_N\}$ and the relative crystallinity is denoted by χ.

Since the order parameters are interpreted as the volume fractions of the corresponding sub-regions, the summation constraint $\sum_{\alpha=1}^{N} \phi_\alpha(\boldsymbol{x}, t) = 1$ has to be fulfilled where $\boldsymbol{x}$ is the position vector, and t is the time.

Subsequently, an additive decomposition of the free energy density is assumed:

$$f(\boldsymbol{\phi}, \nabla\boldsymbol{\phi}, \chi) = f_{\mathrm{int}}(\boldsymbol{\phi}, \nabla\boldsymbol{\phi}) + f_{\mathrm{b}}(\boldsymbol{\phi}, \chi), \tag{2}$$

with f_{int} as the interfacial contribution and f_{b} the bulk contribution. The interfacial contribution consists of the potential and gradient contributions,

$$f_{\mathrm{int}}(\phi, \nabla\ \phi) = f_{\mathrm{pot}}(\phi) + f_{\mathrm{grad}}(\phi, \nabla\ \phi). \tag{3}$$

Following,[37] we consider a gradient contribution f_{grad} of the following form

$$f_{\mathrm{grad}}(\boldsymbol{\phi}, \nabla\boldsymbol{\phi}) = \epsilon \sum_{\beta=2}^{\mathrm{N}} \sum_{\alpha=1}^{\beta-1} \gamma_{\alpha\beta} \left(\phi_\alpha \nabla\phi_\beta - \phi_\beta \nabla\phi_\alpha\right).\left(\phi_\alpha \nabla\phi_\beta - \phi_\beta \nabla\phi_\alpha\right) \tag{4}$$

where $\gamma_{\alpha\beta}$ is the interfacial energy density between two phases, and ϵ is a constant related to the width of the diffuse interface.[38] Since it allows for stabilized interface kinetics[39] and it is numerically more efficient, we use a multi-obstacle potential for the potential contribution f_{pot},

$$f_{\mathrm{pot}} = \frac{16}{\epsilon\pi^2} \sum_{\beta=2}^{\mathrm{N}} \sum_{\alpha=1}^{\beta-1} \gamma_{\alpha\beta} \phi_\alpha \phi_\beta \tag{5}$$

Anywhere the order parameters do not fulfill the Gibbs simplex, given by

$$\mathcal{G} = \left\{ \phi : \sum_{\alpha=1}^{\mathrm{N}} \phi_\alpha(\boldsymbol{x}, t) = 1,\ \phi_\alpha \geq 0\ \forall \alpha \right\}, \tag{6}$$

$f_{\mathrm{pot}} = \infty$ is enforced. The bulk free energy f_{b} is defined as the interpolation of the phase-specific bulk free energies

$$f_{\mathrm{b}} = \sum_{\alpha} \phi_\alpha f_{\mathrm{b}}^{\alpha}(\chi_\alpha), \tag{7}$$

where f_{b}^{α} is the bulk free energy of phase α and it depends on the relative crystallinity of the corresponding phase. The phase-specific bulk free energy for each phase is defined as a quadratic function of the difference between relative crystallinity χ_α and its equilibrium value χ_α^{eq}, i.e. $f_{\mathrm{b}}^{\alpha}(\chi_\alpha) = A_\alpha(\chi_\alpha^{eq} - \chi_\alpha)^2$ where A_α is the driving force coefficient of phase α.

Evolution equation of the order parameter. In this work, the order parameter evolution is described by

$$\frac{\partial \phi_\alpha}{\partial t} = -\frac{1}{\epsilon \mathrm{N}^*} \sum_{\alpha \neq \beta}^{\mathrm{N}^*} M_{\alpha\beta} \left(\frac{\delta \mathcal{F}}{\delta \phi_\alpha} - \frac{\delta \mathcal{F}}{\delta \phi_\beta} \right) \tag{8}$$

where $M_{\alpha\beta}$ is the individual mobility for each $\alpha - \beta$ interface.[40] The mobility of the phase-field evolution can be set to that of a Hoffman-Lauritzen type model[41] to have the growth of the crystalline area to be consistent with the folded-chain crystal models. We further discuss the exact form of the mobility used in our model in section 4.1. The variational derivatives in equation (8) are evaluated using the Euler-Lagrange equation.[42]

Heat Conduction and crystallization

Heat conduction. Processing of thermoplastics always involves heat transfer. Therefore, it is crucial to account for its impact on crystallization. As crystallization is an exothermic phase transition, it is important to account for the heat generated during the process. In the present model, the heat source term that accounts for the crystallization enthalpy depends on the crystallization and cooling rates. Thus, the equation of heat conduction reads

$$\frac{\partial \theta}{\partial t} = \frac{\kappa}{\rho C_v} \nabla^2 \theta + \frac{X_\infty \Delta H_f(\dot{\theta})}{C_v} \frac{\partial \overline{\chi}}{\partial t} \tag{9}$$

where θ is temperature, and $\nabla^2\theta$ denotes the Laplacian of the temperature field. $\kappa(\phi)$ is the phase dependent heat conductivity coefficient, and $C_v(\phi)$ is the phase dependent specific heat. The phase dependent parameters are linearly interpolated at the interface. The numerical values of these parameters can be found in Table 4. The second term on the right hand side of equation (9) is the heat source term where X_∞ is the maximum crystallinity coefficient, $\Delta H_f(\dot{\theta})$ is the cooling-rate dependent crystallization enthalpy. The dependency of the crystallization enthalpy on the cooling rate is found by fitting

experimental data. The local average crystallinity $\overline{\chi}$ is defined as the interpolation of the phase dependent crystallinities:

$$\overline{\chi} = \sum_{\alpha} \chi_{\alpha} \phi_{\alpha} \tag{10}$$

where ϕ_{α} is the phase-field order parameter associated with phase α.

Crystallization model. The multiphase-field model, discussed above, tracks the boundaries of the crystalline regions, i.e. where crystallization can happen and where it cannot. The degree of crystallinity inside the crystalline regions evolves following the Nakamura model. The Nakamura model can be directly derived from the Avrami model assuming a constant ratio of nucleus growth rate to spontaneous nucleation rate (isokinetic condition).[43] We use the differential form of the Nakamura model to track the degree of crystallinity in the crystalline areas[44]

$$\frac{\partial \chi_{\alpha}}{\partial t} = n_{\alpha} K_{\alpha}(\theta, \dot{\theta}\,)(1 - \chi_{\alpha}) \left(\ln\left(\frac{1}{1 - \chi_{\alpha}} \right) \right)^{(n_{\alpha}-1)/n_{\alpha}} \tag{11}$$

where χ_{α} is the crystallinity of phase α, n_{α} is the Avrami coefficient, and K_{α} is the crystallization rate constant which is a function of temperature and its rate of change. K_{α} is typically associated with the crystallization half-time and can be found from experimental data through a half-time analysis.[44] There are empirical[45] and theoretical[41] equations that describe the relation between half-time and temperature. In this work, we use Ziabicki's empirical formulation for our crystallization rate constant[45]

$$K_{\alpha}(\theta, \dot{\theta}\,) = K_{max,\alpha}(\dot{\theta}\,) \exp\left(-4\ln(2) \frac{(\theta - \theta_{max,\alpha})^2}{D_{\alpha}^2} \right). \tag{12}$$

here, the parameters $K_{max,\alpha}$, $\theta_{max,\alpha}$, and D_{α} can be found by fitting DSC measurements, as described in the subsequent sections. This equation has been successfully used in modelling similar systems.[46,47]

Governing equations. The governing equations of our model are collated in Table 1 for convenience.

Table 1. The governing equations, constituting the non-local crystallization model in this work, are the evolution of the order parameter, the equation of heat conduction, and the differential form of the Nakamura model.

Phase-field evolution	$\frac{\partial \phi_{\alpha}}{\partial t} = -\frac{1}{\epsilon N^{*}} \sum_{\alpha \neq \beta}^{N^{*}} M_{\alpha\beta} \left(\frac{\delta \mathcal{F}}{\delta \phi_{\alpha}} - \frac{\delta \mathcal{F}}{\delta \phi_{\beta}} \right)$
Heat conduction	$\frac{\partial \theta}{\partial t} = \frac{\kappa}{\rho C_v} \nabla^2 \theta + \frac{X_{\infty} \Delta H(\dot{\theta}\,)}{C_v} \frac{\partial \overline{\chi}}{\partial t}$
Crystallinity evolution	$\frac{\partial \chi_{\alpha}}{\partial t} = n_{\alpha} K_{\alpha}(\theta, \dot{\theta}\,)(1 - \chi_{\alpha}) \left(\ln\left(\frac{1}{1 - \chi_{\alpha}} \right) \right)^{(n_{\alpha}-1)/n_{\alpha}}$

Experimental data and results

Material information

As an example of thermoplastic material, we use polyamide 6 (PA6). PA6 is a thermoplastic commonly used in the automotive industry, due to its toughness, rigidity, and comparably high service temperature.[48] TechnylStar XS 1352 BL PA6 was purchased from DOMO Chemicals GmbH (Leuna, Germany). Granules of weight of approximately 9 mg were used as samples. Since polyamide is a hygroscopic polymer and therefore tends to absorb water, the samples were dried in a vacuum oven at 50°C for 24 h before testing.

DSC measurements

Experimental procedure. Non-isothermal Differential Scanning Calorimetry (DSC) measurements were performed with a Mettler Toldeo DSC 3 series with automatic sample changer according to DIN EN ISO 11357-1 in aluminum trays and nitrogen atmosphere. Measurements were performed at heating and cooling rates of 0.6 K/min, 5 K/min, 20 K/min, and 50 K/min. To reduce the test time, all measurements were performed in a temperature range of 25 °C–250 °C except for the experiments at 0.6 K/min cooling rate. At 0.6 K/min cooling rate, a temperature range of 100 °C–250 °C was investigated. To account for fluctuations in the measurement data, at least two cooling processes were recorded for each cooling rate.

The results of the DSC measurements with cooling rates ranging from 0.6 K/min to 50 K/min are shown in Figure 1 as a plot of heat flow versus temperature.

Results and discussion of DSC measurements. In Figure 1, we observe that an increase in the cooling rate results in broadening of the DSC exotherms plus a significant increase in the DSC signal. The DSC signal is directly correlated with the crystallization rate such that a more pronounced DSC signal is detected at a higher crystallization rate.[49] Therefore, increasing the cooling rate seems to increase the overall rate of crystallization. The temperature where the peak signal is observed at is called the crystallization temperature T_c. We observe a shift of T_c to lower temperatures when the cooling rate is increased. The horizontal shift of the DSC curves to lower temperatures is attributed to the effect of the cooling rate on nucleation.[50]

Crystallization begins after an initial delay which depends on the interplay between the incubation and residence time. The incubation time is the time required for the critical nucleus to form at that specific temperature. Dependent upon temperature, incubation time is longer at higher temperatures. The residence/induction time is the time it takes for the sample to sense the change in the temperature and adjust during a non-isothermal scan. Successful nucleation occurs when the residence time at a given temperature is more than the incubation time at that temperature.[50,51] At lower cooling rates, this criterion is met at higher temperatures and hence the shift to the right in the DSC exotherms. Conversely at higher cooling rates, the residence time is no longer sufficient for stable nucleation at high temperatures and crystallization happens only at lower temperatures.[50]

The absolute crystallinity (also known as the degree of crystallization) of the sample is determined by the ratio

$$X_\infty = \frac{\Delta H_f - \Delta H_{cold}}{\Delta H_0} \times 100, \tag{13}$$

where ΔH_f corresponds to the enthalpy of fusion after the second heating and as shown in Figure 1, it depends on the cooling rate. ΔH_{cold} is the enthalpy released during cold crystallization, and $\Delta H_0 = 204.8\ \mathrm{J\,g^{-1}}$[52] is the enthalpy of fusion of perfect crystals of PA6. It is to be noted that no cold crystallization enthalpy was detected at any cooling rates in our experiments. The calculated X_∞ as well as crystallization temperature T_c and heat of fusion ΔH_f for different cooling rates are collated in Table 2.

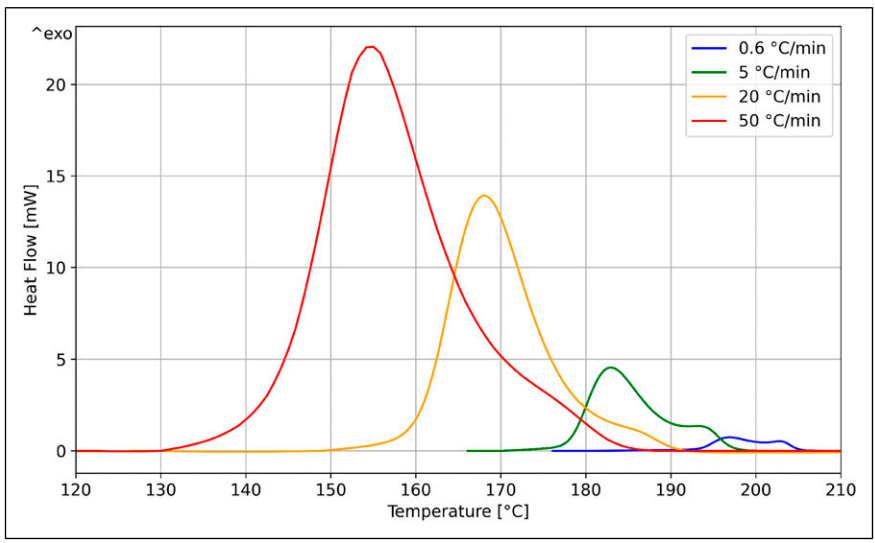

Figure 1. Non-isothermal DSC exotherms are shown at various cooling rates: (red) 50 K/min, (orange) 20 K/min, (blue) 5 K/min, and (purple) 0.6 K/min. The increase in cooling rate results in stronger signals, and lower crystallization temperature.

Table 2. Crystallinity properties for PA6 for different cooling rates.

Cooling rate ($\mathrm{K\,min^{-1}}$)	T_c (°C)	ΔH_f ($\mathrm{J\,g^{-1}}$)	X_∞ (%)
0.6	196.9	67.22	32.8
5	183.2	58.17	28.4
20	168.88	62.28	30.4
50	156.61	55.20	26.9

Light microscopy experiments

Optical microscopy is a powerful method in analyzing the crystalline structure, defects, and orientation of materials such as polymers, liquid crystals, and semiconductors. Polarized light microscopy (PLM) is used in particular to examine crystals.[53–57] In PLM, the light from a transmitted light microscope passes through two polarization filters, each rotated by 90°, which ensure that the light is extinguished in the final image. In contrast to amorphous areas, crystals are optically anisotropic or birefringent objects which, when introduced into the beam path between the polarizers, cause a change in the plane of polarization. As a result, complete extinction no longer occurs and corresponding structures become visible. Hence, we utilize PLM with an integrated cooling/heating chamber to study the impact of cooling rate on spherulite size and distribution as well as the crystallization rate and crystallization temperature range.

Experimental setup and procedure. Thin slices of thickness 7 µm were made from a granulate grain of PA6. This was done using a rotary microtome (HM 355 S, ThermoFisher Scientific). To avoid any undesirable reflections or refractions, the slices were wetted with kerosene oil before being placed on the slide. The temperature chamber was located externally and connected by a tube to the test area under the optical microscope, so that cooling could be performed directly under the microscope.

Experiments were performed on two samples. Each sample was heated and cooled at three different cooling rates: 50 K/min, 20 K/min and 5 K/min. The PLM was conducted using transmitted light with crossed polarizers on a BX-51 (Olympus) machine. In addition, a $\lambda/4$ plate was used to improve contrast. In images taken with a $\lambda/4$-plate, amorphous regions appear as magenta, while the crystalline regions generally appear as yellow or blue, depending on the orientation of the crystallites in the beam path. The microscopy images were taken at 9 frames per second (fps) at 50x magnification. In the generated videos, the temperature was superimposed.

Results and discussion of microscopy experiments. Figure 2 shows the evolution of crystallization at the cooling rate 5 K/min captured by PLM. The images are chronologically arranged from left to right. We initially see a uniform magenta colour indicating that the entire sample is amorphous and liquid. Further cooling of the sample results in formation of crystalline regions. This can be seen in the middle image where several yellow regions appear. These regions seem to form linear stripes. The cooling is continued until no change in the structure of the sample is detected. The final structure of the sample is shown in the image on the right. The yellow stripes already visible in the second image are more pronounced, and the formerly magenta-coloured areas appear as blue dots. In the solid state, therefore, crystalline phases of either orientations (appearing in yellow or blue) have formed in the amorphous areas.

We observe that most of the crystallization sites form instantaneously at a start temperature followed by a relatively rapid growth. The stripe-like patterns of crystals were originally assumed to be the result of sample preparation. However, even after melting the sample and performing cooling experiments, these stripe-like crystalline areas are

observed. This leads us to believe that such patterns are formed following the grooves of the cover glasses/slides. This is further confirmed after comparing the results to the experiments performed at 50 K/min cooling rate.

Figure 3 shows PLM snapshots of the sample cooled at 50 K/min. Like before, the images are chronologically ordered from left to right. Similar stripes of crystalline areas are observed and they seem to form very early on in the crystallization process. However, we see slightly finer and milder yellow regions in the images for 50 K/min cooling rate. This is expected as the polymer chains do not have sufficient time to form folded crystals at high cooling rates resulting in smaller crystals.

There are advantages to using PLM but there are also barriers. Generally, in PLM images, it can be difficult to distinguish between different regions due to the changes caused by rotation of the sample. When the sample is rotated in the beam path, the colours of the crystalline regions interchange, and overall it could be difficult to clearly delineate amorphous and crystalline regions, especially in the presence of fine crystals.

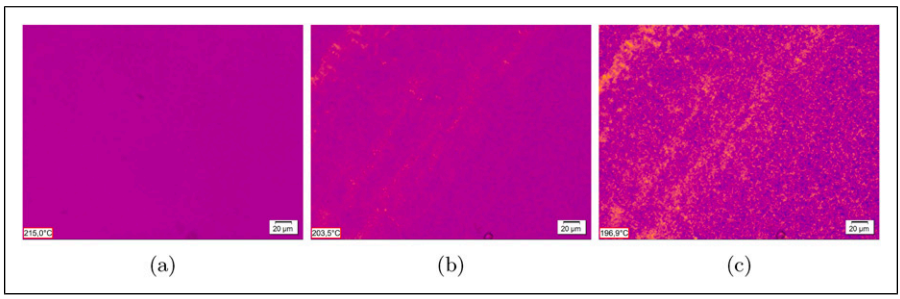

Figure 2. Images of a sample cooled down at 5 K/min (a) initial state (θ = 215°C), (b) during the crystallization process (θ = 203.5°C) and (c) final state (θ = 196.9°C, after no change in the crystallization structure can be seen anymore.) Yellow and blue regions show crystalline areas while magenta demonstrates amorphous regions.

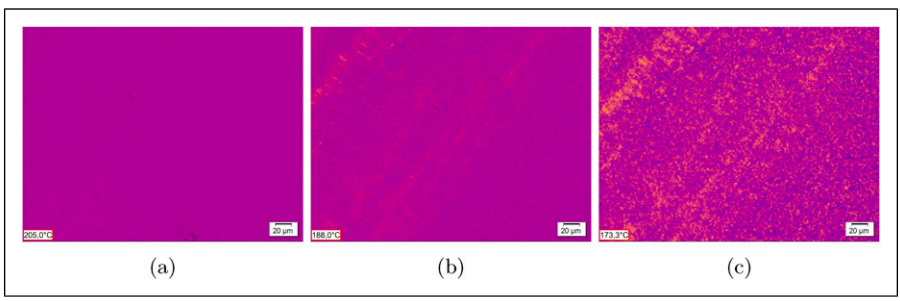

Figure 3. Images of a sample cooled down at 50 K/min (a) initial state (θ = 205°C), (b) during the crystallization process (θ = 188°C) and (c) final state (θ = 173.3°C). Yellow and blue regions show crystalline areas while magenta demonstrates amorphous regions.

Moreover, we could not obtain detailed material characteristic information of the star-branched PA6 used in our experiments. However, we suspect that the 7 μm thickness of our samples is probably considerably larger than a single crystal layer.[58] This can lead to superposition effects during imaging and some errors in the analysis of the images.

Numerical studies and results

Numerical implementations

Determination of crystallization parameters using Ziabicki model. In 1968, Ziabicki extended the Turnbull-Fisher model to describe the kinetics of systems with anisotropic nuclei in isothermal and non-isothermal conditions.[45] Later, he further generalized his model to account for transient and athermal effects.[45] The extended crystallization kinetics function takes the form of a Gaussian function with the empirical parameters K_{max}, D and θ_{max}. The parameters could also be presented as cooling rate-dependent functions by evaluating the DSC measurements for different cooling rates and fitting the parameters on a power function for D and θ_{max}, and a linear function for K_{max} as suggested by Sierra et al.[59] Since the crystallization enthalpy is also shown to be cooling rate-dependent, the term dH could also be linearly fitted in the same way. The crystallization rate constant parameter $K_c(\theta, \dot{\theta})$ takes the form:

$$K_c(\theta, \dot{\theta}) = K_{max,c}(\dot{\theta}) \exp\left(-4\ln(2)\frac{(\theta - \theta_{max,c}(\dot{\theta}))^2}{D_c(\dot{\theta})^2}\right) \tag{14}$$

where subscript c stands for the crystalline phase and

$$\theta_{max,c}(\dot{\theta}) = C_1 \times \dot{\theta}^{-C_2} \tag{15a}$$

$$K_{max,c}(\dot{\theta}) = C_3 \times \dot{\theta} + C_4 \tag{15b}$$

$$D_c(\dot{\theta}) = C_5 \times \dot{\theta}^{C_6} \tag{15c}$$

$$dH(\dot{\theta}) = -C_7 \times \dot{\theta} + C_8. \tag{15d}$$

The value of the coefficients above are shown in Table 3. A plot of K_c as a function of temperature for different cooling rates is shown in Figure 4. To validate these values, the

Table 3. Crystallization parameters for the Ziabicki model (equation (14)) obtained from fitting the DSC measurements.

C_1 [1/s]	C_2 [−]	C_3 (s/K)	C_4 [1/s]	C_5 [1/s]	C_6 [−]	C_7 (s/K)	C_8 (J/kg)
430.15	0.0207	0.0679	0.0063	29.78	0.2596	14.5	67.07

crystallization evolution predicted by the Nakamura model using the fitted coefficients are compared to the experimental results. Figure 5 shows the relative crystallinity as a function of temperature (a) and time (b). The solid lines indicate the results of the Nakamura model using our fitted coefficients and the cross points indicate the experimental data (measured as explained in 3).

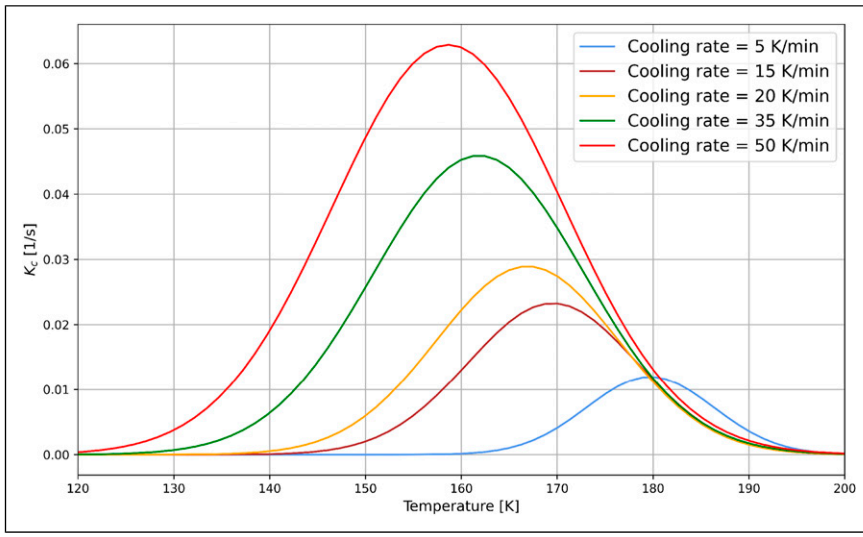

Figure 4. K_c parameter for different cooling rates as a function of temperature. The parameter is derived from the fitted empirical parameters. A clear trend of higher amplitude, wider base and a shift of the curves to the left is shown as the cooling rate increases.

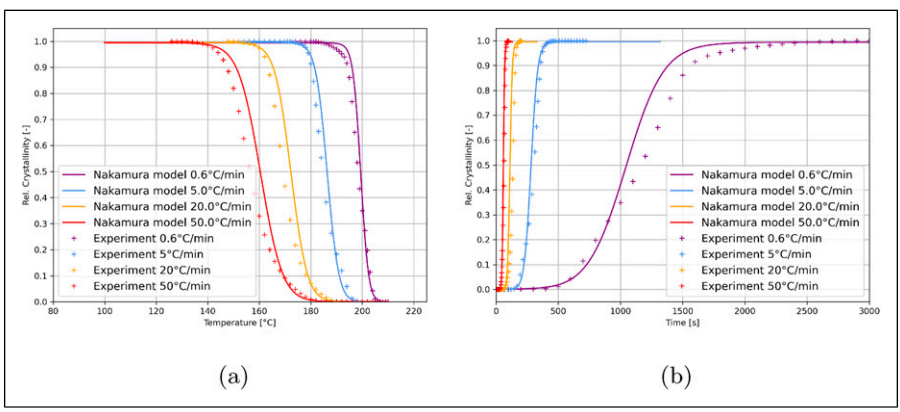

Figure 5. Empirical crystallization parameters are validated by comparing the experimental results to the predictions of the model.

Numerical implementation. As mentioned in the theory section, our model consists of the heat conduction equation, the multiphase-field equation, and the Nakamura equation. The heat conduction and Nakamura equations are discretized using an implicit finite difference method. As the Nakamura model contains nonlinear terms, an iterative Newton method is utilized to find the crystallinity values.

The phase-field evolution equation is explicitly discretized using a second-order finite difference method. To avoid interface pinning and premature grain shrinkage, the driving force coefficient A_c (for crystal phase) in equation (2.1) is calibrated to always fulfill

$$\frac{|\Delta W_{bulk}^{\alpha\beta}|}{\frac{\gamma_{\alpha\beta}+\gamma^n}{\varepsilon}} \approx 1 \tag{16}$$

where $|\Delta W_{bulk}^{\alpha\beta}|$ is the driving force due to crystallization. $\gamma_{\alpha\beta}$ and γ^n are the surface tension in the tangential and normal directions, respectively. The value of A_c also directly affects the critical radius of the grains, meaning that the critical radius decreases when a larger A_c is applied. Figure 6 shows the relation between A_c and the critical radius. This is expected as a larger driving force can overcome the higher surface tension of smaller crystalline grains.

In equation (2.1), the equilibrium crystallinity χ_α^{eq} is assumed to be 1, driving the system towards the maximum crystallinity. This means that initially, when crystallinity is low, we get the highest driving force and the driving force vanishes when full crystallinity is achieved.

We use a mobility M_{ca} between the crystalline and amorphous phase that is a function of the temperature and cooling rate, and has the same shape as the crystallization rate constant K. In order to improve the stability of the phase-field evolution a stabilizing factor is multiplied by the normalized K_c giving rise to the mobility

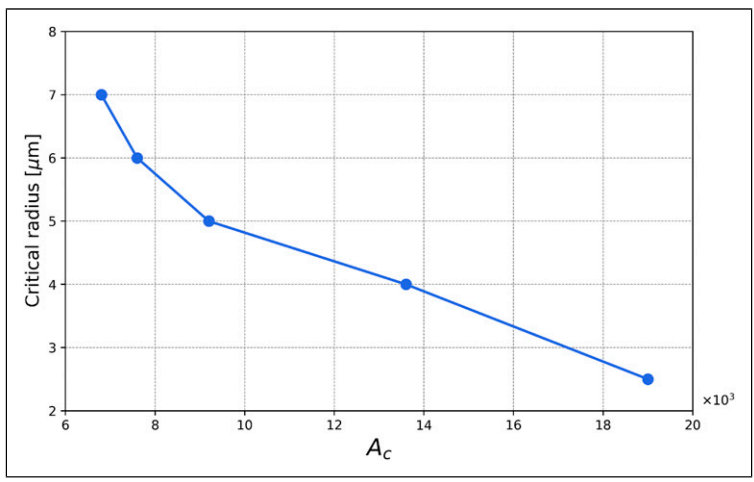

Figure 6. Graph relating the driving force prefactor (A_c) to critical radius.

$$M_{ca} = \frac{(\Delta x)^2}{4\Delta t(\gamma_{ca} + \gamma^n)} \frac{K_c(\theta, \dot{\theta})}{K_{max,c}(\dot{\theta})} \tag{17}$$

where K_c is the crystallization rate constant for the crystal phase (see equation (14)), and $K_{max,c}$ is the crystallization parameter obtained from equation (15b)).

The mobility between the PA6 phases (crystalline and amorphous) and the fiber phase, $M_{\alpha f}$, is considered to be 0. This ensures the stability of the fiber phase and prevents the polymeric phases from leaking into and taking over areas occupied by the fiber phase. The details of the numerical values for each parameter can be found in Table 4.

Table 4. Summary of all model parameters.

Parameter	Value	Unit
Thermal properties		
Thermal conductivity (κ)		
PA6	0.25[60]	W/(m· K)
Carbon fiber	100[61]	W/(m· K)
Specific heat capacity (C_p)		
PA6 (100% amorphous)	512	J/(kg· K)
PA6 (100% crystalline)	4310[a]	J/(kg· K)
Carbon fiber	700[61]	J/(kg· K)
Density (ρ)		
PA6	1130[62]	kg/m^3
Carbon fiber	1800[61]	kg/m^3
PA6 crystallinity properties		
T_{max}	Equation 15(a)	K
D	Equation 15(c)	K
K_{max}	Equation 15(b)	s^{-1}
Phase-field parameters		
Surface tension (PA6)		
Normal component (γ^n)	37.19[63]	mN/m
Tangential component ($\gamma_{\alpha\beta}$)	0.4·(γ^n)	mN/m
Mobility ($M_{\alpha\beta}$)		
PA6	Equation (17)	-
Carbon fiber	0	-
Numerical parameters		
Mesh size	0.5, 1	μm
Box size	500	Cells
Time step	0.01	s
Diffuse interface width	4	Cells

[a]Linearly approximated from 100% amorphous and 30% crystalline.

In this work, we only consider instantaneous formation of crystalline regions at $t = 0$, i.e. crystalline regions are initially distributed in the amorphous phase. It is worth mentioning that the initial crystalline grains are not crystal nuclei but regions that have several crystal nuclei and have the potential to crystallize. Since the Nakamura equation, which controls the degree of crystallinity of the crystalline areas, has to be non-zero to get any evolution, we initialize the crystallinity of the crystalline regions to a very small non-zero value.

The crystallinity only evolves in the crystalline phase and does not evolve in the amorphous phase nor the fiber phase. However, since the mobility between the amorphous and crystalline phase is not zero, the crystal grains can grow into and take over amorphous regions where the crystallization can then take place.

Pure matrix

Single grain. We begin by investigating the simplest system consisting of a single crystalline grain in 2D. The crystalline grains in our coarse-grained model do not correspond to single spherulite but regions with several spherulites. The initial radius of the grain is 6 μm and the initial temperature of the domain is set to 200°C. A Dirichlet boundary condition with a constant cooling rate is applied to the left and right boundaries, while the top and bottom boundaries are periodic. As mentioned before, an initial non-zero value of crystallinity is required for the crystallinity to evolve according to Nakamura model. Thus, we set the initial crystallinity degree of the crystalline areas to the small value 0.1%. As a result, the crystalline areas should not be interpreted as crystal nuclei but regions where some nuclei germs exist and there is potential for crystallization. Figure 7 shows the phase-field order parameter field (upper row) and crystallinity field (lower row) after reaching the glass transition temperature T_g for different cooling rates, namely, 5, 20, 35, and 50 K/min. As can be seen, at higher cooling rates, the final size of the crystalline area is smaller compared to lower cooling rates. As the grain grows, the crystallinity evolves in the newly acquired areas by a rate determined by the temperature and cooling rate at these new areas. As crystallization at different locations happens at different times and temperatures, different levels of crystallinity are observed even inside a crystalline phase, leading to inhomogeneous crystallinity distributions.

The temperature field at different times during the simulation for the cooling rate of 20 K/min is shown in Figure 8. At the beginning, the temperature field is more or less uniform stripes (in the vertical direction). After onset of crystallization, we observe higher temperatures around the crystalline area as a result of the released crystallization heat. As we reach the end of the simulation and crystallization slows down, we see the temperature gradient going back to an almost uniform pattern of stripes. We would like to point out that the effect of the crystallization heat is reduced by the influence of a Dirichlet boundary conditions which are predominant for a simulation box of this size.

Case I: Large grains. The primary goal of this study is to develop a model that is capable of predicting the microstructure of semi-crystalline polymers and capturing the heterogeneous nature of such microstructures. Therefore, the natural next step is to study systems

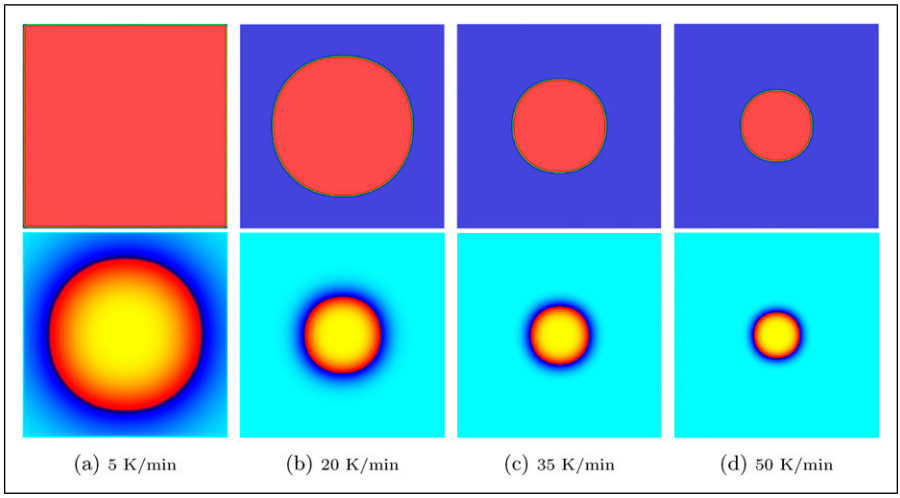

Figure 7. The final morphologies of a single grain under different cooling rates are illustrated. The top row shows the phase-field order parameter field where red shows crystalline areas and blue shows amorphous areas. The bottom row shows the crystallinity field where the aqua blue indicates the amorphous region and the circles in the centre are the crystalline areas. Yellow shows the highest degree of crystallinity and dark blue shows lowest degree of crystallinity. The simulations are done in 2D.

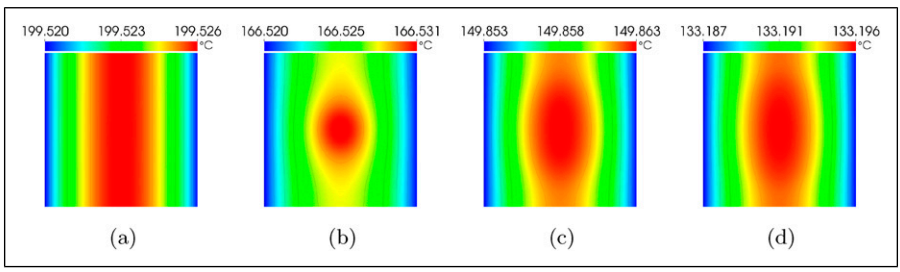

Figure 8. The evolution of the temperature field for cooling rate 20 K/min is shown. (a) t = 5 s, relative crystallinity ≈0 (b)t = 100 s, relative crystallinity = 0.003 (c)t = 150 s, relative crystallinity = 0.54 (d)t = 200 s, relative crystallinity = 1.

with multiple grains and the resulting microstructures. In this section, we investigate the crystallization behaviour of pure PA6 by simulating a 2D system of 500 × 500 cells and $dx = 1$ μm under different cooling rates. The cooling rates selected for this study as with the single grain, are 5 K/min, 20 K/min, 35 K/min, and 50 K/min. Initially, 100 crystalline grains of radius between 4 and 10 μm and initial crystallinity degree of 0.1% are randomly dispersed in the amorphous phase leading to an initial crystal grain volume fraction of 6%. The initial morphology of the system is shown in Figure 9(a).

Figure 10 shows the final (after reaching T_g) morphology of the system for different cooling rates. At the lowest cooling rate of 5 K/min, we observe fewer but larger grains covering almost the entire simulation box. We also see fewer grain boundaries. This is expected as the slower cooling rate provides sufficient time for the grains to grow and enough time for crystallinity to reach high values everywhere. As we increase the cooling rate, we see that the size of the grains becomes smaller and gradients in crystallinity increase leading to fine grain morphologies. This prediction of the impact of cooling rate

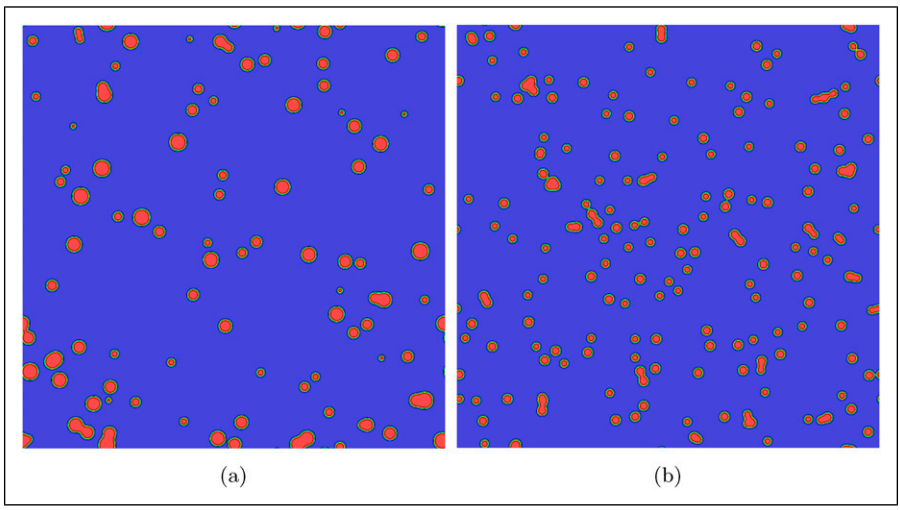

Figure 9. The initial configuration of the system is shown for (a) 100 grains of radius between 4 and 10 μm (b) 185 grains of radius 2.5 and 3 μm. The grains are randomly distributed in the system. The simulations are done in 2D. The red circles are crystalline regions. The crystalline areas should not be interpreted as crystal nuclei but regions where some nuclei germs exist and there is potential for crystallization.

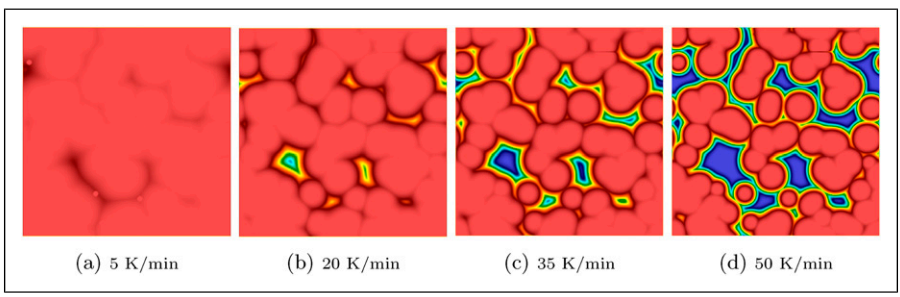

Figure 10. Final morphologies under different cooling rate are shown. System is initialized with 100 grains of radius between 4 and 10 μm (6% area density). As expected, a higher conversion rate and larger crystalline areas are observed for lower cooling rates.

on morphology agrees with what we see in the experiments (see section 3.2) and other experimental work.[50,64]

Case II: Small grains. To study the impact of initial grain structure on the final results, we examine the crystal morphology of pure PA6 for a system with higher number of initial crystalline grains and smaller radii. Initially, we randomly disperse 185 crystalline grains of radii between 2.5 and 3 μm, and initial crystallinity of 0.1%. This gives a similar initial crystal grain volume fraction as the previous example (6%). We apply and study the system under the same cooling rates as before. The simulation box is in 2D with 500×500 cells and $dx = 0.5$ μm. The initial morphology of the system is shown in Figure 9(b).

Figure 11 shows the final morphology of the system for different cooling rates. Similar to the other examples we have discussed so far, we see larger grains and more uniform crystallinity inside each grain when the cooling rates are lower. Increasing cooling rates results in smaller grains and larger variability in the crystallinity field.

Comparing the results in Figures 10 and 11, in general, we see that more of the system crystallizes when more but smaller grains are embedded initially. However, we observe a more distinct difference between the morphologies in Figures 10 and 11 at higher cooling rates. This is due to the fact that at lower cooling rates, the crystallinity has time to evolve to values near 1. Moreover, the temperature gradient across the simulation box is less steep and crystallization heat release is more uniform across the simulation box. All of these results in a more uniform growth of the grains and their crystallinity. In this case, the initial size of the grains has less of an impact compared to the number of initial grains on the total crystallinity as most grains reach their maximum size (considering impingement constraints).

Alternatively at high cooling rates, the number of initial grains and their size both play an important role in the final morphology. In this case, the grains do not have ample time to grow and are smaller in size. Also, due to the rapid decrease of temperature at the boundaries, there are steeper gradients across the simulation box. The combination of

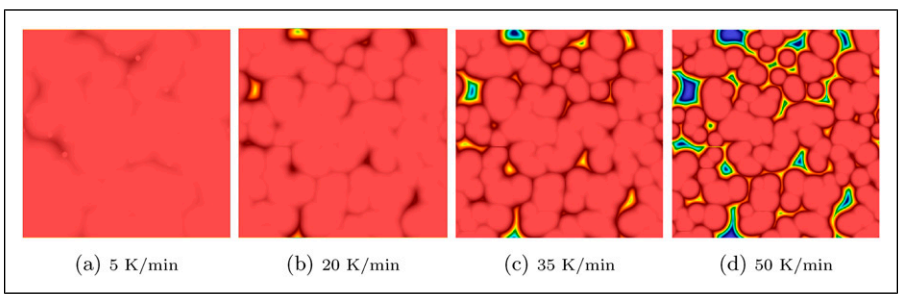

Figure 11. Typical morphologies (after reaching T_g) for a system initialized with 185 crystalline grains of radius between 2.5 and 3 μm and at different cooling rates. At low cooling rates, a more uniform morphology is obtained while more inhomogeneous structures are observed for high cooling rates. Note that the box size is half of the one in Figure 10.

these leads to more localized crystallization (i.e. limited to the location of the initial grains) and therefore more heterogeneity in the morphology.

Relative crystallinity. So far we discussed the resulting morphologies of our simulation and the impact of initial size and distribution of crystalline grains as well as cooling rate on these morphologies. It is informative to look at the relative crystallinity of our systems too as it can directly be compared to the results obtained from our DSC measurements. Figure 12 shows the evolution of the relative crystallinity for case I and case II discussed above. The solid lines show the results of the simulations and the cross points show the results of the DSC measurements. The relative crystallinity is defined as the average crystallinity over the simulation box divided by the maximum:

$$\widehat{\chi} = \frac{\langle \overline{\chi} \rangle}{max\{\overline{\chi}\}} \tag{18}$$

where

$$\langle \overline{\chi} \rangle = \frac{1}{A} \int_A \overline{\chi} da \tag{19}$$

with A denoting the area of the simulation domain. As can be seen, our model correctly recovers the form of the crystallinity evolution curves. We also observe that lowering cooling rates results in the crystallization starting later and taking longer which is consistent with experimental DSC data. The gap between different curves grows as the cooling rate is decreased similar to the experimental curves. However, our model predicts a longer delay prior to the onset of crystallization compared to the experiments (a shift to the right). This difference is present in Figure 5 but it is considerably smaller. Thus, this could be due to ignoring the smaller peaks that are observed in the DSC exotherms at the beginning of crystallization. Moreover, to compare the impact of cooling rate on the final

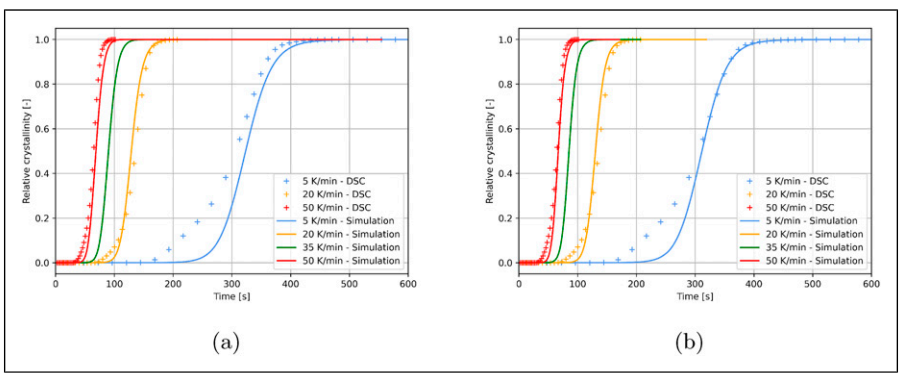

Figure 12. The evolution of relative crystallinity obtained from simulations are compared to DSC results at different cooling rates. (a) is initialized with 100 crystalline grains while (b) is initialized with 185 crystalline grains. The curves provide qualitative agreements with experiments.

morphology, we initialized all systems with similar density of grains, range of radii, and initial degree of crystallinity. In reality, the cooling rate and processing method affect the nucleation process as mentioned in section 3. One would expect higher number of nuclei for systems with higher cooling rates[50] and we observe a better agreement with the experimental results for the system with larger number of initial grains (see Figure 12(b)). The influence of nucleation is included through the Nakamura equation. However, further investigation on the relation between nucleation and initial crystalline grain distribution is required to obtain quantitatively accurate results, which will be investigated in future work.

The relation between relative crystallinity and temperature is also commonly investigated to collect information about crystallization process. Figure 13 shows the relative crystallinity as a function of temperature obtained from our simulations. Similar to evolution plots, we see a good qualitative agreement with Figure 5. The shape of the curves and their order matches the experimental results. However, a shift to lower temperatures is observed in this case. We believe this has the same origin as the shift in the relative crystallinity evolution curves. Comparing Figures 13(a) and (b), we can clearly see the impact of the initial conditions. The curves for the system with lower number and larger size of grains is slightly shifted to higher temperatures and the slope of the curves are marginally less steep.

Particle size distribution. To quantify the size of the crystal grains, continuous particle size distributions (PSD) according to Münch and Holzer are utilized.[65] This method has been successfully used to investigate microstructral properties of nickle coarsening in the multiphase-field context.[66]

The continuous particle size distribution corresponds to the relative volume/area of a certain phase that can be covered by spheres/circles of a certain diameter. The circles are allowed to overlap but they cannot cross the boundaries of the phase. The PSD takes the

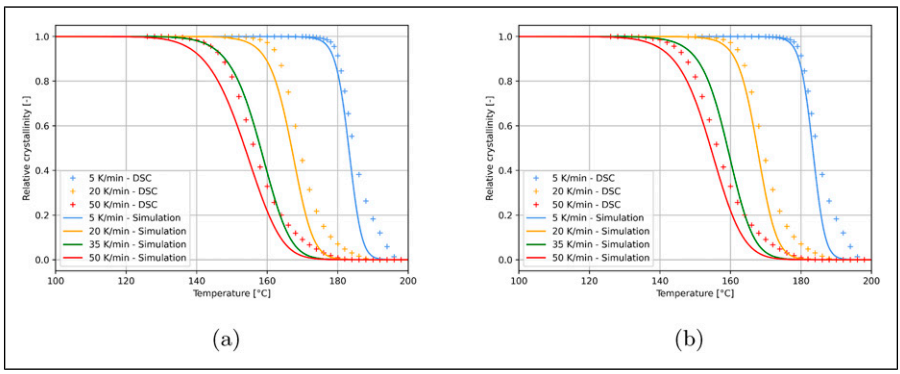

Figure 13. Relative crystallinity is shown as a function of temperature for different cooling rates. The results obtained from our model and DSC measurements are compared. (a) is initialized with 100 crystalline grains while (b) is initialized with 185 crystalline grains. The curves provide qualitative agreements with experiments.

theoretical value of 1 for small enough circles (in practice, the maximum depends on the spatial resolution of the mesh). As the diameter of the circles increases, the PSD decreases since sharp features of the microstructure cannot be swept with large circles. Beyond a certain diameter, it would be impossible to fit any circles inside the phase and PSD becomes zero. Therefore, the continuous particle distribution corresponds to a complementary cumulative distribution taking values between 1 and 0. The probability density function can then be calculated from the negative slope of the continuous PSD. In the current work the density is calculated from the cumulative distribution by finite differences which leads to a histogram dataset.

Figure 14 shows the PSD density function for the two previously discussed cases (large and small initial grains). Figure 14(a)–(d) show the PSD density for the system with large initial grains and at different cooling rates. Each plot shows the PSD density function at

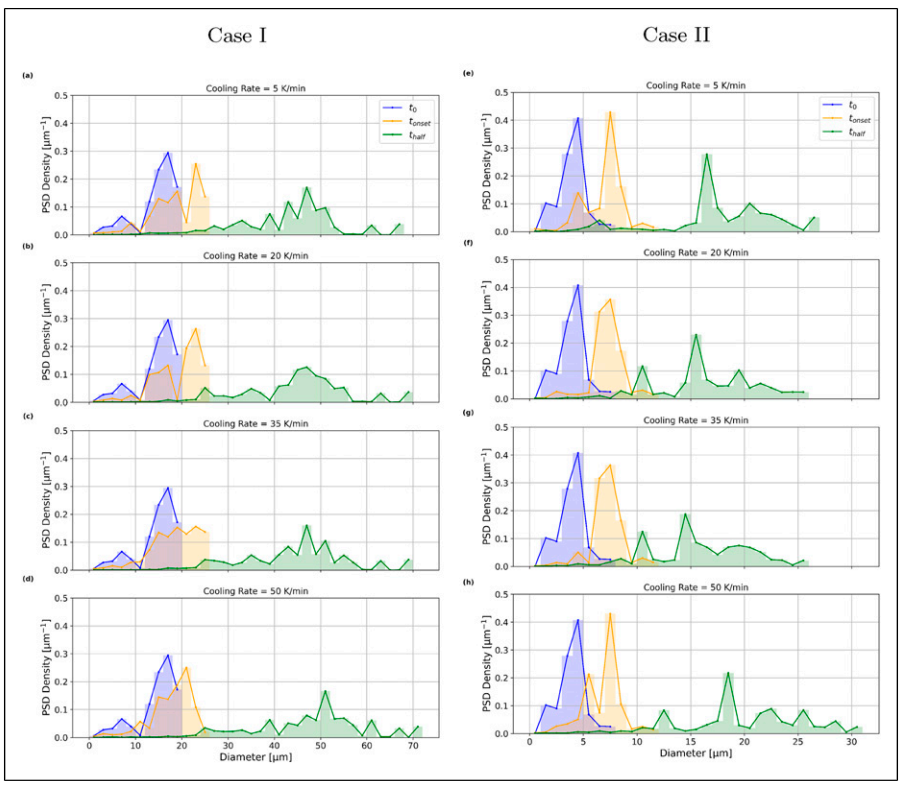

Figure 14. The particle size distribution (PSD) density is shown for case I (left column) and case II (right column). (a)-(d) show the PSD density for cooling rates 5 K/min, 20 K/min, 35 K/min, 50 K/min, respectively. Similarly, (e)-(h) show the PSD density for cooling rates 5 K/min, 20 K/min, 35 K/min, 50 K/min, respectively. The blue graphs is the PSD density at $t = t_0 = 0$s, the orange graphs shows the PSD density at $t = t_{onset}$, and the orange graphs shows the PSD density at $t = t_{half}$. t_{onset} is the time corresponding to when $\widehat{\chi} = 0.01$ and t_{half} corresponds to when $\widehat{\chi} = 0.5$.

3 different times, at the beginning (t_0) , at onset of crystallization (when $\widehat{\chi} = 0.01$), and halfway through crystallization ($\widehat{\chi} = 0.5$). $\widehat{\chi} = 0.01$ is selected to indicate "onset of crystallization" as the changes in the microstructure and the particle size distribution is small prior to this point. At the onset of crystallization, we observe a shift in the distribution to larger diameters. As different grains grow at different rates, depending on their location, heterogeneity, evident by new peaks, also emerges. As time goes on and more crystallization occurs a wider distribution and several peaks are observed. As expected, we see more peaks at higher cooling rates corresponding to more heterogeneity in the microstructure.

Figure 14(e)–(h) show the PSD density for case II (small initial grains) and at different cooling rates. Each plot shows the PSD density function at 3 different times, at the beginning (t_0) , at onset of crystallization (when $\widehat{\chi} = 0.01$), and halfway through crystallization ($\widehat{\chi} = 0.5$). Similar to case I, a shift in the distribution to larger diameters and emergence of new peaks is observed at the onset of crystallization. At t_{half}, a wider distribution and several peaks are observed. Compared to case I, we see a narrower range of grain sizes and smaller grains. This is expected as the initial grain sizes and their distribution were smaller for case II.

In both cases, we see that at $t = t_{half}$, more grains with large diameters are found at cooling rate 50 K/min compared to other cooling rates. This is expected as at higher cooling rates, the system reaches its highest rate of crystallization earlier. However, at higher cooling rates, the crystallization rate drops very quickly thereafter and therefore the final crystal grains are smaller compared to systems that are cooled at lower rate.

Inclusion of fibers

In this section we include different orientations a single discontinuous carbon fiber with a diameter of 7.5 μm and length of 150 μm in a PA6 matrix. The fiber is added to the multiphase-field model as a third phase that does not crystallize. As mentioned before, the mobility between the fiber and the other two phases (amorphous and crystalline) is 0. The thermal properties for the carbon fiber are shown in Table 4. The presence of fiber in a polymer matrix affects the nucleation process of the polymer. The surface of the fiber acts as a local nucleation site for the polymer around it. This phenomenon is called transcrystallinity. To account for this, we initialize the area at the interface and around the fiber in our simulations with a higher density of crystalline grains. We populate the interface of the fiber and the matrix with a maximum of 50% crystallinity. This value is chosen somewhat arbitrarily as we did not have access to experimental data for the specific matrix and fiber used in our experiments. This parameter can be simply adjusted for different systems and upon access to experimental or molecular data. The areas away from the fiber are initialized with 6% volume fraction of the crystalline grains similar to the pure matrix simulations.

Single fiber. Here, we look at a single fiber placed horizontally in the centre of the box. Figure 15 shows the initial and final distribution of grains for a typical system with the horizontal fiber. Results for two cooling rates, 25 K/min and 50 K/min, are shown. The

higher number of initial grains inevitably lead to higher crystallinity around the fiber. The effect of the cooling rate discussed in the previous sections can also be seen here. The lower cooling rate allows for more time for the grains to grow and crystallize leading to less defined boundaries between them. On the other hand, the higher cooling rate exhibits more obvious heterogeneity in the crystallinity field.

Also, we observe that shape of the grains and their boundaries are perpendicular to the fibers. Figure 16(a) shows an enhanced version of Figure 15(b). The grains near the fiber

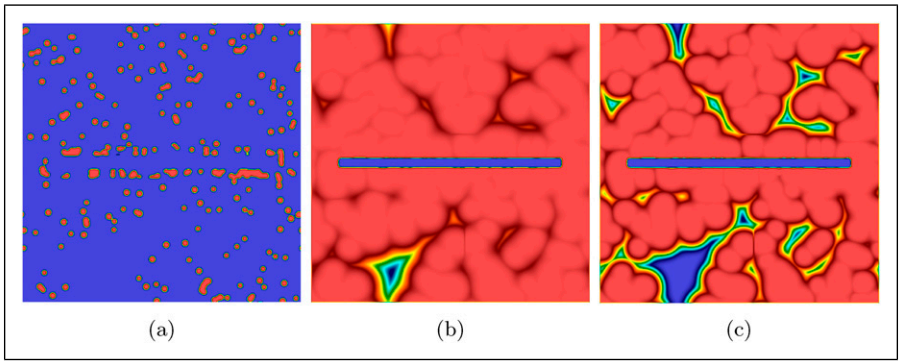

Figure 15. Initial and final morphology for crystallization field around a carbon fiber horizontally placed in the centre of the 2D domain. The carbon fiber has width of 7.5 μm and length of 150 μm. (a) Initial distribution, (b) 25 K/min, (c) 50 K/min. The area at the interface and around the fiber is initialized with a higher density of crystalline grains to account for transcrystallinity. The initial grains are dispersed randomly.

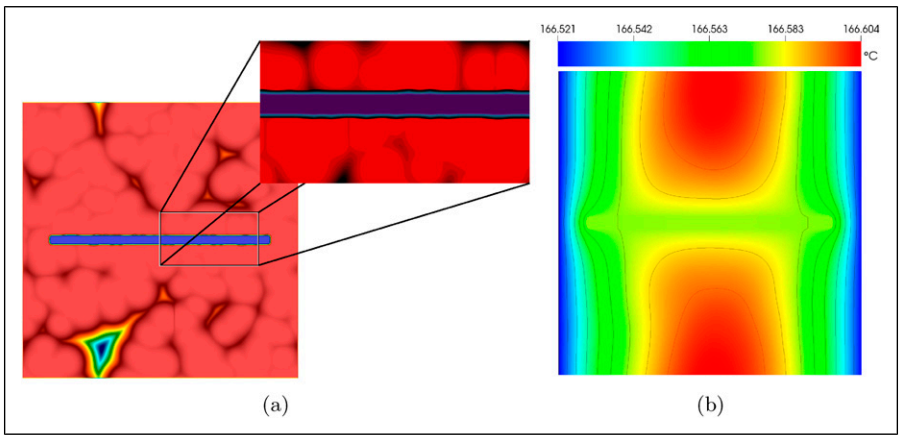

Figure 16. A magnified image of the fiber is shown in (a). Vertical boundaries are observed between grains at the fiber interface. (b) shows the temperature field for a system with a horizontal carbon fiber. Lower temperatures are observed where the fiber is located. This is due to the higher heat conductivity of the fiber compared to the polymer matrix.

take ellipsoidal shapes and the boundaries between them create vertical curves. This behaviour has also been observed in experimental works.[67,68] We do not introduce any source of preferred directionality in our model. Thus, it seems that such patterns appear merely due to geometrical constraints imposed by neighbouring grains and the fiber surface (the grain has no other space to grow except for perpendicular to the fiber and outwards).

The fiber also affects the heat conduction and the temperature field as it has different thermal properties compared to the matrix material. Figure 16(b) shows the temperature field for a system with a horizontal carbon fiber in the centre of the box. The cooling rate for this system was 25 K/min. The carbon fiber has a higher thermal conductivity and a lower volumetric heat capacity than the PA6 matrix around it. The fiber acts as a heat conductor between the right and left boundaries of the domain and facilitates heat flow. This leads to lower but more uniform temperatures at and around the fiber. As a result, we expect a more uniform crystallization rate, especially around the fiber, leading to more homogeneous morphologies. We would like to point out that due to the small gradients of temperature in our system this effect is subtle. However, one can expect more significant influence on the morphology for larger systems or different material properties.

Conclusion

Physical and mechanical properties of semi-crystalline polymers depend on their degree of crystallization and crystal morphology. In this work, we introduce a multiphase-field method coupled with the Nakamura model and heat conduction equation to model the non-local crystallization of polymeric materials on a microstructural length scale. The multiphase-field base of our model provides an efficient and easy way to track the boundaries of the crystalline areas. This makes it possible to study heterogeneous crystal structures. It also allows for adding any number of phases with different properties making the model a good candidate to study polymer blends and composites. The crystallization inside crystalline areas is controlled by a kinetic model, which was the Nakamura model in this work. The dependency of the crystal growth rate on temperature is added by a Turnbell-Fisher type of equation. The kinetic model and temperature dependency can be adjusted to match the processing conditions and specific materials under study.

We applied our model to neat PA6 and in the presence of fibers. For pure matrix, we observe that lower cooling rates result in more homogeneous structures with larger grains. More heterogeneous structures emerge as the cooling rate is increased. This heterogeneity stems from sharper temperature gradients and the short crystallization time available to the crystalline grains. At lower cooling rates, the initial size of the grains does not have a major impact on the final morphology as enough time is given for most grains to grow to their possible maximum crystallinity, considering impingement constraints. The initial number of grains does seem to have a more noticeable effect on the morphology. At higher cooling rates, both of these quantities seem to influence the final structure considerably.

In the presence of the carbon fiber, we observe a more homogeneous morphology around the fiber. This is associated with two effects: higher initial crystal grain volume

fraction and high conductivity of the carbon fibers. All the crystalline grains near the fiber surface experience a similar cooling rate and crystallize at the same rate. The heat of crystallization is also transferred quickly from the region. The higher initial crystal grain volume fraction also means that most regions start crystallizing at the same time. These lead to the more homogeneous morphologies observed around the fiber. We also observe formation of boundaries perpendicular to the fiber between the grains at the fiber interface as they grow.

Overall, our model provides results qualitatively in agreement with experiments. However, further understanding of the properties of the coarse-grained crystal grains and their relation to spherulites, and a detailed knowledge of the initial nuclei density is required to achieve better quantitative agreement with experiments.

Acknowledgements

This work was supported by the Natural Science and Engineering Council of Canada (NSERC) Discovery grant (CD) and a CREATE grant (NA) on Advanced Polymer Composite Materials and Technologies. JB and BS gratefully acknowledge the funding and AP, KAW, and NA gratefully acknowledge the financial support by the Deutsche Forschungsgemeinschaft (DFG, German Research Foundation), project number 255730231, within the International Research Training Group ”Integrated engineering of continuous-discontinuous long fiber reinforced polymer structures” (GRK 2078). DS and BN gratefully acknowledge the financial support of ”Materials Science and Engineering (MSE)” programme No. 43.31.01, supported by the Helmholtz association. AP and AE gratefully acknowledge the financial support by the Bundesministerium für Bildung und Forschung (BMBF, Federal Ministry of Education and Research) within the joint project ”05M2022 - DASEA-4-SOFC”. The support by the German Research Foundation (DFG) is gratefully acknowledged. All microscopy and cooling experiments were conducted at Fraunhofer ICT with the help of Daniel Mitró whose support the authors are extremely thankful for. Sincerest thanks for the provision of the polyamide 6 material by DOMO and to Christoph Schelleis and colleagues at Fraunhofer ICT.

Author contributions

Navid Afrasiabian: Conceptualization; investigation; methodology; formal analysis; visualization; project administration; writing - original draft; writing - editing and review. **Ahmed Elmoghazy:** Parameter identification; methodology; simulation; visualization; writing - original draft; writing - editing and review. **Juliane Blarr:** Experiments; writing - original draft. **Benedikt Scheuring:** Parameter identification; experiments; writing - original draft. **Andreas Prahs:** Supervision; conceptualization; project administration; methodology; writing - editing and review. **Daniel Schneider:** Supervision; conceptualization; project administration; methodology; writing - original draft. **Wilfried V. Liebig:** Supervision; funding acquisition; writing - original draft. **Kay A. Weidenmann:** Supervision; funding acquisition; writing - original draft. **Colin Denniston:** Supervision; funding acquisition; Conceptualization; writing - original draft; writing - editing and review. **Britta Nestler:** Supervision; funding acquisition; writing - original draft.

Declaration of conflicting interests

The author(s) declared no potential conflicts of interest with respect to the research, authorship, and/or publication of this article.

Funding

The author(s) disclosed receipt of the following financial support for the research, authorship, and/or publication of this article: This work was supported by the Bundesministerium für Bildung und Forschung; 05M2022 - DASEA-4-SOFC, Natural Sciences and Engineering Research Council of Canada; CREATE 401209347, Deutsche Forschungsgemeinschaft; 255730231 and Materials Science and Engineering (MSE); 43.31.01.

ORCID iDs

Navid Afrasiabian https://orcid.org/0000-0003-0639-770X
Juliane Blarr https://orcid.org/0000-0003-0419-0780
Andreas Prahs https://orcid.org/0000-0002-8112-9994
Daniel Schneider https://orcid.org/0000-0002-9250-2918
Colin Denniston https://orcid.org/0000-0002-6723-0455

References

1. Afrasiabian N, Balasubramanian V and Denniston C. Dispersion and orientation patterns in nanorod-infused polymer melts. *J Chem Phys* 2023; 158(5): 054902. DOI: 10.1063/5.0122174.
2. Mallick PK. Fiber-reinforced composites: materials. In: *Manufacturing, and ddesign*. 3 edition. Boca Raton, FL: CRC Press, 2007. DOI: 10.1201/9781420005981.
3. Schöller L, Nestler B and Denniston C. Modeling of a two-stage polymerization considering glass fibre sizing using molecular dynamics. *Nanoscale Adv* 2023; 5(1): 106–118. DOI: 10.1039/D2NA00562J.
4. Böhlke T, Henning F, Hrymak A, et al. *Continuous–discontinuous fiber-reinforced polymers: an integrated engineering approach*. Cincinnati, OH, US: Carl Hanser Verlag GmbH & Company KG, 2019. ISBN 978-1-56990-693-4.
5. Meyer N, Hrymak AN and Kärger L. Modeling short-range interactions in concentrated Newtonian fiber bundle suspensions. *Int Polym Process* 2021; 36(3): 255–263. DOI: 10.1515/ipp-2020-4051.
6. Ruan C, Ouyang J and Liu S. Multi-scale modeling and simulation of crystallization during cooling in short fiber reinforced composites. *Int J Heat Mass Tran* 2012; 55(7-8): 1911–1921. DOI: 10.1016/j.ijheatmasstransfer.2011.11.046.
7. Bahloul A, Doghri I and Adam L. An enhanced phase field model for the numerical simulation of polymer crystallization. *Pol crystallization* 2020; 3(4): e10144. DOI: 10.1002/pcr2.10144.
8. Li W, Teo HWB, Chen K, et al. Mesoscale simulations of spherulite growth during isothermal crystallization of polymer melts via an enhanced 3D phase-field model. *Appl Math Comput* 2023; 446: 127873. DOI: 10.1016/j.amc.2023.127873.

9. Zhang MC, Guo BH and Xu J. A review on polymer crystallization theories. *Crystals* 2017; 7(1): 4. DOI: 10.3390/cryst7010004.
10. Zhang J and Muthukumar M. Monte Carlo simulations of single crystals from polymer solutions. *J Chem Phys* 2007; 126(23): 234904. DOI: 10.1063/1.2740256.
11. Shen C, Zhou Y, Chen J, et al. Numerical simulation of crystallization morphological evolution under nonisothermal conditions. *Polym-Plast Technol Eng* 2008; 47(7): 708–715. DOI: 10.1080/03602550802129676.
12. Kundagrami A and Muthukumar M. Continuum theory of polymer crystallization. *J Chem Phys* 2007; 126(14): 144901. DOI: 10.1063/1.2713380.
13. Huang T and Kamal MR. Morphological modeling of polymer solidification. *Polym Eng Sci* 2000; 40(8): 1796–1808. DOI: 10.1002/pen.11311.
14. Frank FCI. I. Liquid crystals. On the theory of liquid crystals. *Discuss Faraday Soc* 1958; 25: 19. DOI: 10.1039/df9582500019.
15. Molnár J, Sepsi Ö, Gaál B, et al. Probabilistic numerical simulation for predicting spherulitic morphology from calorimetric crystallization conversion curves: an isothermal case. *Mater Des* 2021; 212: 110245. DOI: 10.1016/j.matdes.2021.110245.
16. Chen LQ. Phase-field models for microstructure evolution. *Annu Rev Mater Res* 2002; 32: 113–140. DOI: 10.1146/annurev.matsci.32.112001.132041.
17. Steinbach I. Phase-field models in materials science. *Model Simulat Mater Sci Eng* 2009; 17(7): 073001. DOI: 10.1088/0965-0393/17/7/073001.
18. Moelans N, Blanpain B and Wollants P. An introduction to phase-field modeling of microstructure evolution. *Calphad* 2008; 32(2): 268–294. DOI: 10.1016/j.calphad.2007.11.003.
19. Xu H, Matkar R and Kyu T. Phase-field modeling on morphological landscape of isotactic polystyrene single crystals. *Phys Rev* 2005; 72(1): 011804. DOI: 10.1103/PhysRevE.72.011804.
20. Wang XD, Ouyang J, Su J, et al. A phase-field model for simulating various spherulite morphologies of semi-crystalline polymers. *Chin Phys B* 2013; 22(10): 106103. DOI: 10.1088/1674-1056/22/10/106103.
21. Kobayashi R. Modeling and numerical simulations of dendritic crystal growth. *Phys Nonlinear Phenom* 1993; 63(3): 410–423. DOI: 10.1016/0167-2789(93)90120-P.
22. Taguchi K, Miyaji H, Izumi K, et al. Growth shape of isotactic polystyrene crystals in thin films. *Polymer* 2001; 42(17): 7443–7447. DOI: 10.1016/S0032-3861(01)00215-4.
23. Beers KL, Douglas JF, Amis EJ, et al. Combinatorial measurements of crystallization growth rate and morphology in thin films of isotactic polystyrene. *Langmuir* 2003; 19(9): 3935–3940. DOI: 10.1021/la026751r.
24. Krause T, Kalinka G, Auer C, et al. Computer simulation of crystallization kinetics in fiber-reinforced composites. *J Appl Polym Sci* 1994; 51(3): 399–406. DOI: 10.1002/app.1994.070510302.
25. Mehl NA and Rebenfeld L. Computer simulation of crystallization kinetics and morphology in fiber-reinforced thermoplastic composites. I. Two-dimensional case. *J Polym Sci B Polym Phys* 1993; 31(12): 1677–1686. DOI: 10.1002/polb.1993.090311203.
26. Mehl NA and Rebenfeld L. Computer simulation of crystallization kinetics and morphology in fiber-reinforced thermoplastic composites. III. Thermal nucleation. *J Polym Sci B Polym Phys* 1995; 33(8): 1249–1257. DOI: 10.1002/polb.1995.090330810.

27. Benard A and Advani SG. An analytical model for spherulitic growth in fiber-reinforced polymers. *J Appl Polym Sci* 1998; 70(9): 1677–1687. https://doi.org/10.1002/(SICI)1097-4628(19981128)70:9⟨1677::AID-APP5⟩3.0.CO;2-4.
28. Haudin JM and Chenot JL. Numerical and physical modeling of polymer crystallization: Part I: theoretical and numerical analysis. *Int Polym Process* 2004; 19(3): 267–274. DOI: 10.3139/217.1829.
29. Durin A, Boyard N, Bailleul JL, et al. Semianalytical models to predict the crystallization kinetics of thermoplastic fibrous composites. *J Appl Polym Sci*. 2017; 134(8): 44508–44519. DOI: 10.1002/app.44508.
30. Galeski S, Piorkowska E, Rozanski A, et al. Crystallization kinetics of polymer fibrous nanocomposites. *Eur Polym J* 2016; 83: 181–201. DOI: 10.1016/j.eurpolymj.2016.08.002.
31. Ruan C, Ouyang J, Liu S, et al. Computer modeling of isothermal crystallization in short fiber reinforced composites. *Comput Chem Eng* 2011; 35(11): 2306–2317. DOI: 10.1016/j.compchemeng.2010.11.011.
32. Steinbach I, Pezzolla F, Nestler B, et al. A phase field concept for multiphase systems. *Phys Nonlinear Phenom* 1996; 94(3): 135–147. DOI: 10.1016/0167-2789(95)00298-7.
33. Schöller L, Schneider D, Herrmann C, et al. Phase-field modeling of crack propagation in heterogeneous materials with multiple crack order parameters. *Comput Methods Appl Mech Eng* 2022; 395: 114965. DOI: 10.1016/j.cma.2022.114965.
34. Kannenberg T, Schöller L, Prahs A, et al. Microstructure evolution accounting for crystal plasticity in the context of the multiphase-field method. *Comput Mech* 2023; 74: 67–84. DOI: 10.1007/s00466-023-02423-7.
35. Prahs A, Schöller L, Schwab FK, et al. A multiphase-field approach to small strain crystal plasticity accounting for balance equations on singular surfaces. *Comput Mech* 2023; 73: 773–794. DOI: 10.1007/s00466-023-02389-6.
36. Prahs A, Reder M, Schneider D, et al. Thermomechanically coupled theory in the context of the multiphase-field method. *Int J Mech Sci* 2023; 257: 108484. DOI: 10.1016/j.ijmecsci.2023.108484.
37. Nestler B, Garcke H and Stinner B. Multicomponent alloy solidification: phase-field modeling and simulations. *Phys Rev* 2005; 71(4): 041609. DOI: 10.1103/PhysRevE.71.041609.
38. Herrmann C, Schoof E, Schneider D, et al. Multiphase-field model of small strain elasto-plasticity according to the mechanical jump conditions. *Comput Mech* 2018; 62(6): 1399–1412. DOI: 10.1007/s00466-018-1570-0.
39. Karma A and Rappel WJ. Phase-field method for computationally efficient modeling of solidification with arbitrary interface kinetics. *Phys Rev* 1996; 53(4): R3017–R3020. DOI: 10.1103/PhysRevE.53.R3017.
40. Steinbach I and Pezzolla F. A generalized field method for multiphase transformations using interface fields. *Phys Nonlinear Phenom* 1999; 134(4): 385–393. DOI: 10.1016/S0167-2789(99)00129-3.
41. Hoffman JD, Davis GT and Lauritzen JI. The rate of crystallization of linear polymers with chain folding. In: NB Hannay (ed) *Treatise on solid state chemistry: volume 3 crystalline and noncrystalline solids*. Boston, MA: Springer US, 1976, pp. 497–614. DOI: 10.1007/978-1-4684-2664-9_7.

42. Goldstein H, Poole C and Safko J. *Classical mechanics*. San Francisco, CA, US: Addison Wesley, 2002. ISBN 978-0-201-65702-9.
43. Nakamura K, Watanabe T, Katayama K, et al. Some aspects of nonisothermal crystallization of polymers. I. Relationship between crystallization temperature, crystallinity, and cooling conditions. *J Appl Polym Sci* 1972; 16(5): 1077–1091. DOI: 10.1002/app.1972.070160503.
44. Patel RM and Spruiell JE. Crystallization kinetics during polymer processing—analysis of available approaches for process modeling. *Polym Eng Sci* 1991; 31(10): 730–738. DOI: 10.1002/pen.760311008.
45. Ziabicki A. Generalized theory of nucleation kinetics. II. Athermal nucleation involving spherical clusters. *J Chem Phys* 1968; 48(10): 4374–4380. DOI: 10.1063/1.1668003.
46. Di Lorenzo ML and Silvestre C. Non-isothermal crystallization of polymers. *Prog Polym Sci* 1999; 24(6): 917–950. DOI: 10.1016/S0079-6700(99)00019-2.
47. Sajkiewicz P. Kinetics of crystallisation of polymers - a review. *Prog Rubber Plast Recycl Technol* 2002; 18(3): 195–215. DOI: 10.1177/147776060201800304.
48. Kutz M. Applied plastics engineering handbook: processing and materials. *PDL handbook series*. Chadds Ford, PA, USA: Elsevier Science, 2011. ISBN 978-1-4377-3514-7.
49. Ehrenstein G, Riedel G and Trawiel P. *Thermal analysis of plastics: theory and PractiVce*. Cincinnati, OH: Carl Hanser Verlag GmbH & Company KG, 2012. US. ISBN 978-3-446-43414-1.
50. Kocic N, Lederhofer S, Kretschmer K, et al. Nucleation parameter and size distribution of critical nuclei for nonisothermal polymer crystallization: the influence of the cooling rate and filler. *J Appl Polym Sci*. 2015; 132(6): 41433–41447. DOI: 10.1002/app.41433.
51. Long Y, Shanks RA and Stachurski ZH. Kinetics of polymer crystallisation. *Prog Polym Sci* 1995; 20(4): 651–701. DOI: 10.1016/0079-6700(95)00002-W.
52. Bose S, Bhattacharyya AR, Kodgire PV, et al. Fractionated crystallization in PA6/ABS blends: influence of a reactive compatibilizer and multiwall carbon nanotubes. *Polymer* 2007; 48(1): 356–362. DOI: 10.1016/j.polymer.2006.11.019.
53. Lin Y, Zhong W, Shen L, et al. Study on the relationship between crystalline structures and physical properties of polyamide-6. *J Macromol Sci, Part B* 2005; 44(2): 161–175. DOI: 10.1081/MB-200049762.
54. Yuan M, Turng LS, Gong S, et al. Crystallization behavior of polyamide-6 microcellular nanocomposites. *J Cell Plast* 2004; 40(5): 397–409. DOI: 10.1177/0021955X04047220.
55. Chen N, Yao X, Zheng C, et al. Study on the miscibility, crystallization and crystalline morphology of polyamide-6/polyvinylidene fluoride blends. *Polymer* 2017; 124: 30–40. DOI: 10.1016/j.polymer.2017.07.040.
56. Ferreira T, Lopes PE, Pontes AJ, et al. Microinjection molding of polyamide 6. *Polym Adv Technol* 2014; 25(8): 891–895. DOI: 10.1002/pat.3322.
57. Zhang X, Gohn A, Mendis G, et al. Probing three distinct crystal polymorphs of melt-crystallized polyamide 6 by an integrated fast scanning Calorimetry chip system. *Macromolecules* 2021; 54(16): 7512–7528. DOI: 10.1021/acs.macromol.1c00811.
58. Ferreiro V, Pennec Y and Séguéla R. Shear banding in polyamide 6 films as revealed by atomic force microscopy. *Polymer* 2000; 41(4): 1561–1569. DOI: 10.1016/S0032-3861(99)00276-1.

59. Sierra J, Noriega Escobar M, Gómez J, et al. Isothermal and non-isothermal crystallization kinetics for blends of polyamide 6 and polypropylene. *Zeitschrift Kunststofftechnik/Journal of Plastics Technology* 2006.
60. Mark JE. *Physical properties of polymers handbook*. New York, US: Springer Science & Business Media, 2007. ISBN 978-0-387-69002-5.
61. Kirk RERE, Othmer DFDF, Kroschwitz JI, et al. *Encyclopedia of chemical technology*. 4th edition, New York, NY: Wiley, 1991. ISBN 978-0-471-52669-8.
62. Li M, Wan Y, Gao Z, et al. Preparation and properties of polyamide 6 thermal conductive composites reinforced with fibers. *Mater Des* 2013; 51: 257–261. DOI: 10.1016/j.matdes.2013.03.076.
63. Wang Y, Liu S, Zhu H, et al. The entangled conductive structure of CB/PA6/PP MFCs and their electromechanical properties. *Polymers* 2021; 13(6): 961. DOI: 10.3390/polym13060961.
64. Salmerón Sánchez M, Mathot VBF, Vanden Poel G, et al. Effect of the cooling rate on the nucleation kinetics of poly(l-lactic acid) and its influence on morphology. *Macromolecules* 2007; 40(22): 7989–7997. DOI: 10.1021/ma0712706.
65. Münch B and Holzer L. Contradicting geometrical concepts in pore size analysis attained with electron microscopy and mercury intrusion. *J Am Ceram Soc* 2008; 91(12): 4059–4067. DOI: 10.1111/j.1551-2916.2008.02736.x.
66. Hoffrogge PW, Schneider D, Wankmüller F, et al. Performance estimation by multiphase-field simulations and transmission-line modeling of nickel coarsening in FIB-SEM reconstructed Ni-YSZ SOFC anodes I: influence of wetting angle. *J Power Sources* 2023; 570: 233031. DOI: 10.1016/j.jpowsour.2023.233031.
67. Varga J and Karger-Kocsis J. Interfacial morphologies in carbon fibre-reinforced polypropylene microcomposites. *Polymer* 1995; 36(25): 4877–4881. DOI: 10.1016/0032-3861(95)99305-E.
68. Thomason JL and Van Rooyen AA. Transcrystallized interphase in thermoplastic composites. *J Mater Sci* 1992; 27(4): 889–896. DOI: 10.1007/BF01197638.